

Theory of measurement crosstalk in superconducting phase qubits

A. G. Kofman,^{1,*} Q. Zhang,¹ J. M. Martinis,² and A. N. Korotkov¹

¹*Department of Electrical Engineering, University of California, Riverside, CA, 92521*

²*Department of Physics, University of California, Santa Barbara, CA, 93106*

(Dated: January 25, 2020)

We analyze the crosstalk error mechanism in measurement of two capacitively coupled superconducting flux-biased phase qubits. The damped oscillations of the superconducting phase after the measurement of the first qubit may significantly excite the second qubit, leading to its measurement error. The first qubit, which is highly excited after the measurement, is described classically. The second qubit is treated both classically (using several models) and quantum-mechanically. The results of the analysis are used to find the upper limit for the coupling capacitance (thus limiting the frequency of two-qubit operations) for a given tolerable value of the measurement error probability.

PACS numbers: 74.50.+r, 03.67.Lx, 03.65.Xp, 85.25.Cp

I. INTRODUCTION

Superconducting Josephson-junction circuits, including phase,¹ flux,² and charge³ qubits, have attracted a significant interest as promising devices for quantum information processing.⁴ In this paper we consider flux-biased phase qubits,^{5,6,7} which have been introduced relatively recently and have a clear advantage over the current-biased phase qubits. While the schematic of a flux-biased phase qubit (Fig. 1) may be very similar to a flux qubit (in the simplest case, a superconducting loop interrupted by one Josephson junction), an important difference is that in the phase qubit the logic states are represented by two lowest levels in one well of the corresponding potential profile, while for the flux qubit the levels in two neighboring wells are used. An imaginary-swap quantum gate, which together with single-qubit rotations forms a universal set of quantum gates,⁸ has been realized with flux-biased phase qubits in Ref. 9.

Simultaneous measurement of all the qubits is an important stage in quantum information processing, representing one of numerous challenges on the way to a scalable quantum computer. Recently a scheme allowing for fast simultaneous measurement of two coupled flux-biased phase qubits has been implemented.⁹ According to this scheme, a measurement is performed by lowering the barrier between the shallow (“left”) potential well used for qubit states and a much deeper “right” well (Fig. 1), so that a qubit in the upper state $|1\rangle$ switches by tunneling to the right-hand well with probability close to one, whereas a qubit in the lower state $|0\rangle$ remains intact. Since the qubit coupling is fixed in the common design of superconducting circuits, the measurement is complicated by a crosstalk.⁹ The mechanism of the crosstalk is the following. Suppose that one of the qubits is measured in state $|1\rangle$, which means tunneling to the right well. The tunneling will then be followed by the dissipative evolution (damped oscillations), eventually reaching the ground state of the right well. These oscillations will obviously perturb the state of the second, capacitively coupled qubit, especially because in the experiment the os-

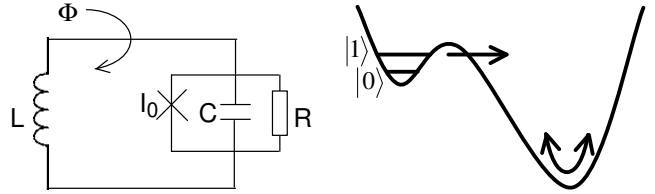


FIG. 1: The circuit schematic of a flux-biased phase qubit and the corresponding potential profile (as a function of the phase difference δ across the Josephson junction). During the measurement the state $|1\rangle$ escapes from the “left” well through the barrier, which is followed by oscillations in the “right” well. This dissipative evolution leads to the two-qubit crosstalk.

cillation frequencies in both wells are close to each other, and both qubits are practically identical. Therefore, if the measurement of the second qubit is made after the dissipative evolution of the first qubit, the measurement result is likely to be wrong (it will practically always be $|1\rangle$ because of the second qubit excitation⁹). To avoid this problem, the measurement of both qubits should be done almost simultaneously,⁹ within the timescale shorter than development of the crosstalk mechanism. However, this is not a complete solution of the problem because the excitation of the second qubit due to crosstalk may be sufficient to switch the qubit from the left well to the right well, even if this excitation happens a little after the second qubit measurement, that will also lead to the measurement error. We emphasize that the above crosstalk is due to a fixed coupling between the qubits. It seems possible that schemes with adjustable coupling can be realized in future, which will eliminate much of the measurement crosstalk discussed here. Still, it is of interest to analyze the fixed-coupling case, since that is the simplest scheme and the only one so far realized experimentally.

The present paper is devoted to the theoretical study of the measurement crosstalk between two capacitively coupled flux-biased phase qubits. In Sec. II we study some basic properties of phase qubits. In particular, the simplified cubic potential is discussed and the Hamilton-

nian for two capacitively coupled qubits is derived. The measurement crosstalk is studied in Secs. III-V. For definiteness, we assume that the first qubit is switched (state $|1\rangle$), whereas the second qubit is initially in the state $|0\rangle$. The dynamics of the first qubit, which after the switching performs damped oscillations in the deep well, is analyzed classically in Sec. III. Such an approximation drastically simplifies the problem and, at the same time, is quite accurate, since for the experimental parameters⁹ used here the first qubit is highly excited after measurement, with typical quantum number over 10^2 . The second qubit in this paper is treated both classically and quantum-mechanically. The classical treatment (Sec. IV) involves two approaches: the harmonic-oscillator model,⁹ which allows for an analytical treatment, and a numerical solution for the exact Hamiltonian. In the quantum approach (Sec. V), an efficient method of numerical solution of the Schroedinger equation, based on using a subset of the eigenstates of the unperturbed Hamiltonian, is developed. The results of the quantum approach are somewhat similar to those of the classical treatment. Our quantum treatment, in contrast to the classical one, does not allow for dissipation in the second qubit, but an insight into possible effects of dissipation can be obtained by the comparison of the two approaches. The conclusions following from the present work are summarized in Sec. VI.

II. FLUX-BIASED PHASE QUBITS

Before the discussion of the basic equations for coupled qubits in Sec. II C, we will dwell on the properties of one qubit in Secs. II A and II B.

A. Qubit potential

A flux-biased phase qubit schematic⁵ coincides with that of the basic rf SQUID¹⁰ (Fig. 1). Neglecting dissipation, it can be described¹⁰ as a fictitious mechanical system with the Hamiltonian

$$H = \frac{p^2}{2m} + U(\delta), \quad (1)$$

where δ is the Josephson-junction phase difference, $p = m\dot{\delta}$ is the corresponding momentum, $m = (\Phi_0/2\pi)^2 C$ is the effective mass determined by the capacitance C , $\Phi_0 = h/(2e)$ is the flux quantum, e is the electron charge, and $U(\delta)$ is the potential energy (shown schematically in Fig. 1)

$$U(\delta) = E_J \left[\frac{(\delta - \phi)^2}{2\lambda} - \cos \delta \right]. \quad (2)$$

Here $E_J = \Phi_0 I_0 / 2\pi$ is the Josephson energy, $\lambda = 2\pi I_0 L / \Phi_0$ is the dimensionless inductance, $\phi = 2\pi\Phi/\Phi_0$

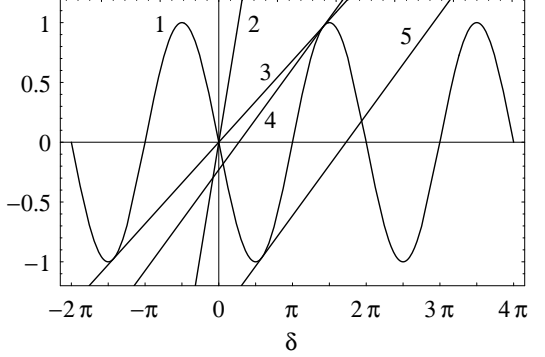


FIG. 2: The graphic solution of Eq. (3); see text.

is the dimensionless external magnetic flux, I_0 is the critical current, and L is the inductance.

In this and the next subsections we review the basic properties¹⁰ (see also⁷) of the potential energy (2). Since the potential is invariant with respect to simultaneous change of δ and ϕ by $2\pi n$ where n is integer, we limit ourselves by the range $0 \leq \phi \leq 2\pi$ for the external flux. Notice that the potential is symmetric for $\phi = n\pi$ ($\Phi = n\Phi_0/2$).

The maxima and minima of the potential (2) satisfy the equation

$$(\delta - \phi)/\lambda = -\sin \delta, \quad (3)$$

which can be solved graphically. Figure 2 shows the r.h.s. of Eq. (3) (curve 1) and the l.h.s. (straight lines 2-5) for several values of the parameters. This equation can have only one solution when the straight-line slope is greater than 1 (as for line 2 in Fig. 2); therefore in the case $\lambda < 1$ the potential (2) has only one well for any external flux ϕ .

For $\lambda > 1$ the potential may have more than one well. There will be at most two wells if the slope of the l.h.s. of Eq. (3) is greater than the slope $1/\lambda_1$ of line 3 in Fig. 2, which is tangent to $-\sin \delta$ at two points $\pm\delta'$ (the line passes through the origin because of the symmetry). This condition yields the equation $\tan \delta' = \delta'$ with the least positive root $\delta'_1 = 4.493$, which corresponds to $\lambda_1 = -1/\cos \delta'_1 = 4.603$. Thus, for λ in the interval¹⁰

$$1 < \lambda < 4.603 \quad (4)$$

the potential has one or two wells depending on ϕ . In particular, for the experimental parameters of Ref. 9 used in this paper [Eq. (12) below] one obtains $\lambda = 3.72$ (as for lines 4 and 5 in Fig. 2), which satisfies condition (4). Similarly, one can show that the potential will have n or $n + 1$ wells (depending on ϕ) if

$$\lambda_{n-1} < \lambda < \lambda_n \quad (n \geq 1), \quad (5)$$

where $\lambda_0 = 1$, $\lambda_n = 1/|\cos \delta'_n|$, and δ'_n is the n th (in the increasing order) positive root of $\tan \delta' = \delta'$. In particular, $\lambda_2 = 7.790$, $\lambda_3 = 10.95$, $\lambda_4 = 14.10$, whereas $\lambda_n \approx (n + 1/2)\pi$ for $n \gg 1$.

The condition for a two-well potential in the case (4) can be found by considering the transition between the one-well and two-well cases, which is illustrated by lines 4 and 5 in Fig. 2. These lines are tangent to $-\sin \delta$ at the points δ_c (critical fluxes) which correspond to the inflection points of the potential (2) (when a well disappears, the corresponding maximum and minimum of the potential merge, so that both the first and second derivatives are zero at this point). Solving the equation for the inflection points

$$\cos \delta_c = -1/\lambda \quad (6)$$

(which does not depend on the external flux), we get two solutions in the interval $(0, 2\pi)$:

$$\delta_c = \pi/2 + \arcsin(1/\lambda), \quad \delta'_c = 2\pi - \delta_c. \quad (7)$$

Inserting these results into Eq. (3), we finally obtain the condition for a two-well potential:

$$\phi'_c < \phi < \phi_c, \quad (8)$$

$$\phi_c = \pi/2 + \sqrt{\lambda^2 - 1} + \arcsin(1/\lambda), \quad \phi'_c = 2\pi - \phi_c \quad (9)$$

(it is easy to show that $\phi'_c < \phi_c$ for $\lambda > 1$).

For definiteness we consider the case $\pi < \phi < \phi_c$, in which the right well is deeper than the left well. The depth $\Delta U_{l,r}$ of a left (l) or right (r) well (i.e., the difference between the potential maximum and minimum) can be characterized by the crude estimate of the number of discrete levels in the well

$$N_{l,r} = \frac{\Delta U_{l,r}}{\hbar \omega_{l,r}}, \quad (10)$$

where $\omega_{l,r}$ is the “plasma” frequency (classical oscillation frequency near the well bottom),

$$\omega_{l,r} = \sqrt{E_J(1/\lambda + \cos \delta_{l,r})/m}, \quad (11)$$

and $\delta_{l,r}$ corresponds to the well minimum and obeys Eq. (3). Notice that $N_{l,r}$ is not necessarily integer and there is no simple relation between $N_{l,r}$ and exact number of discrete levels in the well because of significant anharmonicity of the potential.

In numerical calculations below, we will use the following values of the parameters from the experiment of Ref. 9:

$$C = 700 \text{ fF}, \quad L = 0.72 \text{ nH}, \quad I_0 = 1.7 \mu\text{A}. \quad (12)$$

Figure 3 shows the potential for $N_l = 5$ (corresponding to $\phi = 5.089$). The qubit levels $|0\rangle$ and $|1\rangle$ are, respectively, the ground and the first excited levels in the left well.

B. Cubic potential

When one of the wells is very shallow, it can be approximated by a cubic potential. Assuming $0 < \phi_c - \phi \ll \phi_c$

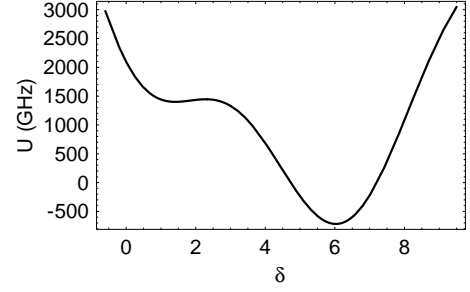


FIG. 3: The qubit potential $U(\delta)$ [Eq. (2)] for $N_l = 5$.

(shallow left well) we can approximate $\cos \delta$ in the vicinity of δ_c as

$$\begin{aligned} \cos \delta &= \cos \delta_c \cos y - \sin \delta_c \sin y \\ &\approx -\lambda^{-1}(1 - y^2/2) - A(y - y^3/6), \end{aligned} \quad (13)$$

where $y = \delta - \delta_c$ and $A = \sqrt{1 - \lambda^{-2}}$. Then the potential (2) can be approximated by the cubic polynomial $U_c(\delta) = AE_J(\epsilon y/2 - y^3/6)$, where a constant is neglected and

$$\epsilon = 2(\phi_c - \phi)/(A\lambda). \quad (14)$$

The minimum and maximum of this potential are at $y_l = -\sqrt{\epsilon}$ and $y_{\max} = \sqrt{\epsilon}$, respectively, i.e., at

$$\delta_l = \delta_c - \sqrt{\epsilon}, \quad \delta_{\max} = \delta_c + \sqrt{\epsilon}. \quad (15)$$

Shifting the axis as $x = y + \sqrt{\epsilon} = \delta - \delta_c + \sqrt{\epsilon}$ and again neglecting a constant, the potential can be rewritten as

$$U_c(\delta) = AE_J(\sqrt{\epsilon}x^2/2 - x^3/6). \quad (16)$$

In this approximation¹⁰ the left well parameters are

$$\begin{aligned} \omega_l &= \epsilon^{1/4} \sqrt{AE_J/m}, \quad \Delta U_l = \frac{2}{3} AE_J \epsilon^{3/2}, \\ N_l &= 2\epsilon^{5/4} \sqrt{mAE_J}/3\hbar. \end{aligned} \quad (17)$$

The validity condition for the cubic-potential description (16) is $\epsilon \ll 1$, which is well satisfied for the left well with qubit parameters considered in the present paper.

C. Two capacitively coupled qubits

Let us consider two capacitively coupled flux-biased phase qubits⁹ (Fig. 4). The current balance for this circuit yields the equations

$$\ddot{\delta}_i + \frac{\dot{\delta}_i}{C'_i R_i} + \frac{2\pi I_{0i}}{\Phi_0 C'_i} \sin \delta_i + \frac{\delta_i - \phi_i}{C'_i L_i} = \frac{C_x}{C'_i} \ddot{\delta}_j, \quad (18)$$

where $i, j = 1, 2$ ($i \neq j$); $C'_i = C_i + C_x$; δ_i , I_{0i} , C_i , and L_i are respectively the Josephson-junction phase difference, critical current, capacitance, and inductance for the i th qubit, C_x is the coupling capacitance, and $\phi_i = 2\pi\Phi_i/\Phi_0$

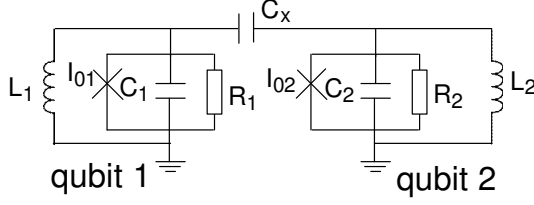


FIG. 4: The circuit schematic for two capacitively coupled flux-biased phase qubits.

is the dimensionless external magnetic flux. Dissipation in Josephson junctions is described here using the resistively shunted junction (RSJ) model,¹⁰ by introducing resistances R_1 and R_2 into the circuit (Fig. 4). For each junction dissipation can be characterized by the energy relaxation time

$$T_1 = R_1 C_1, \quad T'_1 = R_2 C_2. \quad (19)$$

In the absence of dissipation ($R_i = \infty$) Eq. (18) can be written in the form of Lagrange's equations,¹¹

$$\frac{d}{dt} \frac{\partial L}{\partial \dot{\delta}_i} - \frac{\partial L}{\partial \delta_i} = 0, \quad (20)$$

with the Lagrangian

$$L = K - U_1(\delta_1) - U_2(\delta_2). \quad (21)$$

Here the i th qubit potential energy is [cf. Eq. (2)]

$$U_i(\delta_i) = E_{Ji} \left[\frac{(\delta_i - \phi_i)^2}{2\lambda_i} - \cos \delta_i \right], \quad (22)$$

where $E_{Ji} = \Phi_0 I_{0i} / 2\pi$, $\lambda_i = 2\pi I_{0i} L_i / \Phi_0$, and the kinetic energy K is

$$K = \frac{m'_i \dot{\delta}_1^2}{2} + \frac{m'_i \dot{\delta}_2^2}{2} - m_x \dot{\delta}_1 \dot{\delta}_2, \quad (23)$$

where $m'_i = (\Phi_0 / 2\pi)^2 C'_i$ and $m_x = (\Phi_0 / 2\pi)^2 C_x$ are the normalized capacitances. Thus, the problem of two coupled qubits is equivalent to the motion of a fictitious particle in the two-dimensional space (δ_1, δ_2) . From Eqs. (21) and (23) one can obtain the generalized momenta $p_i = \partial L / \partial \dot{\delta}_i$ in the form

$$p_i = m'_i \dot{\delta}_i - m_x \dot{\delta}_j. \quad (24)$$

It is easy to see that p_i is the total charge on the i th junction and the adjacent coupling capacitor multiplied by $\hbar/2e$.^{10,12} Dissipation can be accounted for by the addition¹¹ of the friction force F_i into r.h.s. of Eq. (20). This yields Eq. (18) if

$$F_i = -\frac{\Phi_0^2}{4\pi^2 R_i} \dot{\delta}_i. \quad (25)$$

Equations (24) can be inverted, yielding

$$\dot{\delta}_i = p_i / m''_i + p_j / m'_x, \quad (26)$$

where $m''_i = m_i + (m_j^{-1} + m_x^{-1})^{-1}$ and $m'_x = m_1 + m_2 + m_1 m_2 / m_x$. Inserting Eq. (26) into (23), one obtains the Hamiltonian¹¹ $H = K + U_1 + U_2$ in the form¹³

$$H = \frac{p_1^2}{2m''_1} + \frac{p_2^2}{2m''_2} + \frac{p_1 p_2}{m'_x} + U_1(\delta_1) + U_2(\delta_2). \quad (27)$$

Notice that the Hamiltonian (27) can also be derived in a direct way (without Lagrangian language) using the fact¹⁰ that the node charge (multiplied by $\hbar/2e$) p_i is the conjugated variable to the phase δ_i and expressing the combined electrostatic energy of capacitors C_1 , C_2 and C_x in the form of three first terms of Eq. (27).

Instead of Lagrange's equations (20), one can use Hamilton's equations¹¹ with respect to δ_i and p_i , viz., Eq. (26) and $\dot{p}_i = -\partial H / \partial \delta_i$ or, in view of (27),

$$\dot{p}_i = -\frac{\partial U_i}{\partial \delta_i}. \quad (28)$$

This equation can be extended to take dissipation into account by adding the friction force (25):

$$\dot{p}_i = -\frac{\partial U_i}{\partial \delta_i} - \frac{\Phi_0^2}{4\pi^2 R_i} \dot{\delta}_i. \quad (29)$$

In this paper we mainly consider a system of two identical qubits, then the subscript i can be dropped in the parameter notation:

$$C_i = C, \quad L_i = L, \quad I_{0i} = I_0, \quad R_i = R \quad (30)$$

(the external flux ϕ_i , which is the control parameter in experiments, is assumed to be generally different for the two qubits). Then Eqs. (26) and (27) become

$$H = \frac{p_1^2 + p_2^2 + 2\zeta p_1 p_2}{2(1 + \zeta)m} + U_1(\delta_1) + U_2(\delta_2), \quad (31)$$

$$\dot{\delta}_i = \frac{p_i + \zeta p_j}{(1 + \zeta)m}, \quad (32)$$

where $\zeta = C_x / (C + C_x)$. Experimental parameters of Ref. 9, $C_x = 6$ fF and $T_1 = 25$ ns, correspond to $R = 35.7$ k Ω and $\zeta = 8.5 \times 10^{-3}$.

The above formalism provides a basis for the analysis of the qubit-system evolution before the measurement (the gate operation), during the measurement pulse, and after the measurement pulse (the crosstalk). The latter stage is considered below.

III. MEASUREMENT CROSSTALK: FIRST QUBIT DYNAMICS

In the fast measurement scheme employed in Refs. 9 and 6, a short flux pulse applied to the measured qubit decreases the barrier between the two wells (see Fig. 1), so that the upper qubit level becomes close to the barrier top. In the case when level $|1\rangle$ is populated, there is a

fast population transfer (tunneling) from the left well to the right well. Due to dissipation, the energy in the right well gradually decreases, until it reaches the bottom of the right well. In contrast, if the qubit is in state $|0\rangle$ the tunneling essentially does not occur. The qubit state in one of the two potential minima (separated by almost Φ_0) is subsequently distinguished by a nearby SQUID, which completes the measurement process.

In a system of two identical coupled qubits, crosstalk can produce measurement error if the qubits have different logical states.⁹ For definiteness, we assume that before the measurement the qubit system is in the state $|10\rangle$, i.e., the first qubit is in the excited state and second qubit is in the ground state. Then after the measurement the first qubit performs damped oscillations in the right well, which in the classical language¹⁰ produces an oscillating (microwave) voltage $(\Phi_0/2\pi)\dot{\delta}_1(t)$. This voltage causes oscillating current through the coupling capacitor C_x , which perturbs the second qubit. The effect is so strong that measurement of the second qubit after the dissipative evolution of the first qubit is practically useless: there is almost no chance to find it in the ground state.⁹ The effect of crosstalk can be significantly suppressed if the two qubits are measured practically simultaneously (experimentally, not more than few nanoseconds apart) because the crosstalk excitation of the second qubit takes finite time.⁹ Nevertheless, crosstalk leads to noticeable measurement errors even in the case of simultaneous qubit measurement. The reason is that strong excitation of the second qubit may lead to its switching from the left to the right well even in absence of the measurement pulse.

This is exactly the effect which we analyze in this paper. We assume that the first qubit is switched to the right well at $t = 0$, while the second qubit at this time is in the ground state and no measurement pulse is applied to the second qubit (physically, this means that the pulse is short and does not change the qubit state). Our main goal will be analysis of the measurement error, which in this case is switching of the second qubit to the right well due to the crosstalk excitation.

A rigorous theoretical study of the measurement crosstalk should involve a numerical solution of quantum evolution of two coupled qubits with the account of dissipation, which would require extensive computer resources. In the present paper we employ several simplified approaches, which have the advantage of being relatively fast numerically and thus facilitating a study of the crosstalk dependence on the parameters. The first qubit is always treated classically, whereas the second qubit is studied both classically and quantum mechanically.

We will mainly consider two experimentally relevant cases of the second qubit biasing, characterized by the dimensionless barrier heights $N_{l2} = 5$ or 10 ($\phi_2 = 5.09$ and 4.84 , respectively). Then the plasma frequencies are $\omega_{l2}/2\pi = 8.91$ and 10.2 GHz, respectively. The crosstalk mechanism is obviously very efficient when the first qubit

oscillation is in resonance with ω_{l2} .

For the first qubit we choose the biasing parameter $N_{l1} = 1.355$ ($\phi_1 = 5.31$) which is close to the experimental value^{9,17} at which the state $|1\rangle$ efficiently tunnels out. The corresponding WKB tunneling rate¹⁸ of the state $|1\rangle$ is 3×10^9 s⁻¹, which ensures tunneling during few-nanosecond-long measurement pulse as in experiments of Refs. 6,9. Notice that the barrier height N_{l1} is smaller than the naive estimate 1.5 for the dimensionless energy of the state $|1\rangle$. Actually, because of significant anharmonicity, the energies of states $|0\rangle$ and $|1\rangle$ in this case are 0.475 and 1.26 from the well bottom in units of $\hbar\omega_{l1}$, where $\omega_{l1}/2\pi = 6.87$ GHz. We neglect the fact that in the experiment, after the measurement pulse, the biasing of the left qubit returns back to $N_{l1} \sim 5$, because as we checked, this does not lead to a significant change of the evolution dynamics in the right well.

At the initial moment $t = 0$ the first qubit is assumed to be in the right well close to the barrier top position, with the velocity $\dot{\delta}_1 = 0$. However, instead of assuming its initial energy to be the same as the energy of state $|1\rangle$, we choose a slightly lower energy, which is below the top of the barrier by 20% of the well depth ΔU_{l1} . This (somewhat arbitrary) choice prevents unphysically slow dynamics of a classical particle in the case when it is very close to the barrier top (quantum dynamics due to dissipation does not significantly slow down at the energy close to the barrier top). We have also checked that the qubit dynamics is not too sensitive to the choice of initial energy (if it is above the left well bottom and not too close to the barrier top).

Since the initial energy of the first qubit with respect to the bottom of the right well is much higher than the maximal energy of the second qubit in the left well, one can neglect the back action of the second qubit on the first one while the the second qubit remains in the left well. Then the second term in the numerator in Eq. (32) for the first qubit ($i = 1$) can be dropped, yielding

$$\dot{\delta}_1 = p_1/m'', \quad (33)$$

so Eq. (29) with $i = 1$ gives the approximate equation of motion for the first qubit:

$$\ddot{\delta}_1 + \frac{\dot{\delta}_1}{C''R} + \frac{2\pi I_0}{\Phi_0 C''} \sin \delta_1 + \frac{\delta_1 - \phi_1}{C''L} = 0, \quad (34)$$

where $C'' = (1 + \zeta)C$. This is obviously the usual equation for an isolated first qubit with capacitance C replaced by effective capacitance $C'' = C + C_x C / (C_x + C)$ which takes into account the series connection of the coupling capacitance and the second junction capacitance (this corresponds to the approximation of zero charge at the second qubit).

Note that even though the set of equations of motion (18) is equivalent to Eqs. (26) and (29), the above approximation makes them different. In particular, in the case of identical qubits the equation for the first qubit

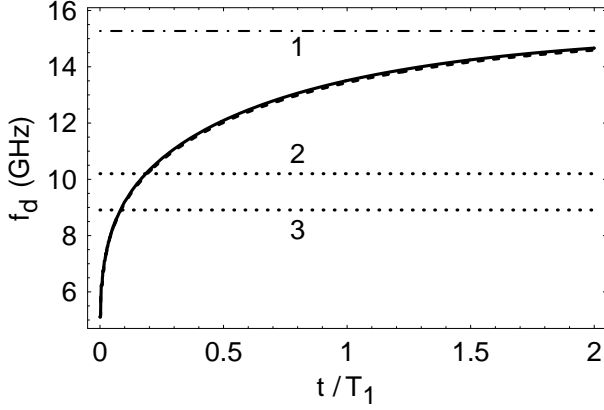


FIG. 5: The first-qubit oscillation frequency f_d as a function of time t/T_1 for $C_x = 0$ (solid line) and $C_x = 6$ fF (dashed line), assuming $N_{l1} = 1.355$ and parameters (12). Horizontal line 1: $\omega_{r1}/2\pi = 15.3$ GHz, the long-time limit of f_d ; line 2: $\omega_{l2}/2\pi = 10.2$ GHz (for $N_{l2} = 10$); line 3: $\omega_{l2}/2\pi = 8.91$ GHz (for $N_{l2} = 5$).

obtained from Eq. (18) by neglecting the r.h.s., differs from Eq. (34) by the substitution $C'' \leftrightarrow C'$. However, for small ζ (which is the experimentally relevant case assumed here), the two equations differ by very small terms on the order of ζ^2 . Physically, $C' = C + C_x$ as the effective capacitance of the first qubit corresponds to the model in which the voltage across the second junction is neglected (in contrast to the charge in the previous model).

Equation (34) shows that the first qubit performs damped non-harmonic oscillations. Because of anharmonicity, the gradual decrease of the qubit energy $E_1 = m''\dot{\delta}_1^2/2 + U_1(\delta_1)$ due to dissipation leads to the gradual increase⁹ of the oscillation frequency f_d (driving the second qubit) which can be obtained as¹¹

$$f_d^{-1}(E_1) = \sqrt{2m''} \int_{a(E_1)}^{b(E_1)} \frac{d\delta_1}{\sqrt{E_1 - U_1(\delta_1)}}, \quad (35)$$

where a and b are the classical turning points. The time dependence $f_d(t)$ of the oscillation frequency is shown in Fig. 5 for $C_x = 0$ (solid line) and 6 fF (dashed line) assuming $T_1 = 25$ ns. The curves are very close to each other showing very small effect of the capacitance renormalization (so that even smaller second-order effect of the difference between C' and C'' is really negligible). We have also checked numerically that variation of T_1 from 25 ns to 500 ns does not change noticeably the dependence $f_d(t)$ if the time is normalized by T_1 , which is rather obvious since $f_d \gg T_1^{-1}$.

Figure 5 shows that the oscillation frequency sharply increases initially and then slowly tends to the right-well plasma frequency $\omega_{r1}/2\pi = 15.3$ GHz. This is explained by the fact that the initial system energy is close to the barrier top, where the oscillation frequency is significantly lower (it tends to zero when the energy approaches

the barrier top), while anharmonicity becomes relatively weak after the energy is no longer close to the barrier top.

Notice that it takes a finite time t_c for the first qubit dynamics to get into resonance with the second qubit ($\omega_{l2}/2\pi$ around 9-10 GHz as mentioned above); we find from Fig. 5 that $t_c = 0.085 T_1$ for $N_{l2} = 5$ and $t_c = 0.192 T_1$ for $N_{l2} = 10$. As a simple estimate, this is the time after which the second qubit becomes significantly excited.⁹

As will be discussed below, the driving force for the second qubit is proportional to $\ddot{\delta}_1(t)$, which can be cast into the form

$$\ddot{\delta}_1(t) = 2A(t) \cos \left(\int^t \omega_d dt \right) + \dots \quad (36)$$

Here $\omega_d = 2\pi f_d$ and the dots stand for the higher-order harmonics, which seem to play a minor role in the second-qubit excitation. The numerical Fourier transform of $\ddot{\delta}_1(t)$ shows that $A(t)$ increases with time, reaches the maximum value 5.8×10^3 ns⁻² at $t = 0.52T_1$, and then decreases. In particular, $A(t_c) = 4.3 \times 10^3$ ns⁻² for $N_{l2} = 5$ and $A(t_c) = 5.2 \times 10^3$ ns⁻² for $N_{l2} = 10$. The initial increase is due to the fact that the oscillation anharmonicity decreases with time, whereas the subsequent decrease of $A(t)$ results from the decrease of the amplitude of the damped oscillation. Note that the above value of $A(t_c)$ for $N_{l2} = 5$ agrees with the rough estimate, $A \simeq \omega_{l2}^2 \tilde{A} = 4.3 \times 10^3$ ns⁻², where $\tilde{A} = 1.36$ is half the amplitude of $\delta_1(t)$ oscillations at the energy corresponding to the exact resonance (121 GHz below the barrier top).

IV. SECOND QUBIT: CLASSICAL APPROACH

In the approximation (33), the second-qubit equation of motion follows from Eqs. (32) and (29) with $i = 2$:

$$\ddot{\delta}_2 + \frac{\dot{\delta}_2}{(1 + \zeta)T'_1} + \frac{2\pi I_0}{\Phi_0 C''} \sin \delta_2 + \frac{\delta_2 - \phi_2}{C'' L} = \zeta \ddot{\delta}_1(t). \quad (37)$$

Here we assume that the second-qubit relaxation time T'_1 may be different from the first-qubit value T_1 . For simplicity we will mostly neglect the energy relaxation for the second qubit ($T'_1 = \infty$), while more experimentally relevant case $T'_1 = T_1$ will be briefly discussed only in the classical approach.

Equation (37) has a simple physical meaning as an evolution of the second qubit with effective junction capacitance C'' , externally driven by the oscillating current $(\Phi_0/2\pi)\zeta C'' \dot{\delta}_1$. However, considering oscillating voltage $(\Phi_0/2\pi)\dot{\delta}_1$ across the first junction coupled to the second qubit via capacitance C_x , one would expect the driving current to be $(\Phi_0/2\pi)C_x \ddot{\delta}_1$. The relative difference between $\zeta C''$ and C_x is on the order of $\zeta^2 \ll 1$, which is the accuracy of treating two qubits separately.

In this section we consider classical dynamics of the second qubit due to the (non-harmonic) oscillating driving force $\zeta\ddot{\delta}_1(t)$ in Eq. (37) with a slowly varying period and amplitude.

A. Harmonic-oscillator model

Though Eq. (37) is simpler than the exact equations (32) and (29), the behavior described by Eq. (37) is still complicated and generally chaotic.¹⁹ To get an insight into the behavior of the second qubit, we first model it by a harmonic oscillator,⁹ i.e., substitute Eq. (37) by

$$\ddot{x} + \omega_{l2}^2 x = \zeta\ddot{\delta}_1(t), \quad (38)$$

where $x = \delta_2 - \delta_{l2}$, δ_{l2} is the left-well minimum position, and ω_{l2} is the unperturbed plasma frequency. Actually, the small-vibration frequency in Eq. (37) is different from ω_{l2} due to the mass (capacitance) renormalization $m \rightarrow m''$, so that $\omega'_{l2} = \omega_{l2}/\sqrt{1+\zeta}$; however, for small coupling considered here ($\zeta \lesssim 1\%$) one can neglect the difference. Correspondingly, the oscillator energy is $E_2 = m''(\dot{x}^2 + \omega_{l2}^2 x^2)/2$.

We have simulated Eq. (38) numerically, assuming the system initially at rest at the potential minimum, $x(0) = \dot{x}(0) = 0$, and checked that the oscillator energy coincides with the analytical solution:¹¹

$$E_2(t) = \frac{\zeta^2 m''}{2} \left| \int_0^t dt' e^{-i\omega_{l2} t'} \ddot{\delta}_1(t') \right|^2. \quad (39)$$

Figure 6 shows the time dependence of the energy $E_2(t)$ in units of $\hbar\omega_{l2}$ for $\omega_{l2}/2\pi = 8.91$ GHz, which corresponds to $N_{l2} = 5$ (parameters of the first qubit evolution have been discussed in Sec. III and correspond to Fig. 5). One can see that the energy E_2 remains very low until a sharp increase followed by oscillations around a value comparable to the maximum. This behavior can be easily explained by changing in time frequency f_d of the driving force (Fig. 5) which passes through the resonance with the second qubit.⁹

For an analytical analysis, let us consider the vicinity of the moment t_c of exact resonance, $\omega_d(t_c) = \omega_{l2}$, and approximate $\ddot{\delta}_1(t)$ as a harmonic signal $\ddot{\delta}_1(t) = A \exp(i \int^t \omega_d dt)$ [cf. Eq. (36)] with constant amplitude $A = A(t_c)$ and linearly varying frequency

$$\omega_d(t) = \omega_{l2} + \alpha(t - t_c), \quad (40)$$

with $\alpha = \dot{\omega}_d(t_c) > 0$ (neglecting the complex conjugated term and higher-order harmonics as being out of resonance). Thus the problem is reduced to passage of a harmonic oscillator through resonance with a constant rate.^{20,21} Also assuming slow crossing, $\alpha \ll \omega_{l2}^2$, and shifting the lower endpoint of integration in Eq. (39) to $-\infty$ (which is a good approximation for $t_c \gg \sqrt{2/\alpha}$), we

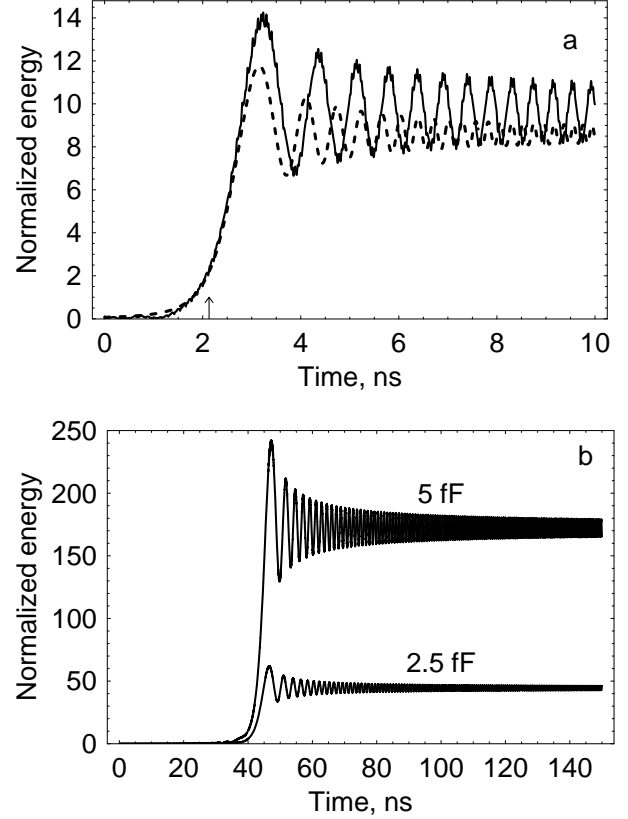


FIG. 6: The oscillator energy E_2 (in units of $\hbar\omega_{l2}$) vs. time t (in ns) for (a) $C_x = 5$ fF and $T_1 = 25$ ns and (b) $C_x = 2.5$ fF and 5 fF and $T_1 = 500$ ns. Dashed line shows approximation using Eq. (41). The arrow shows the moment when the driving frequency shown in Fig. 5 is in resonance with ω_{l2} .

obtain

$$E_2(t) = E_0 F(\tilde{t}), \quad E_0 = \frac{\pi \zeta^2 m'' A^2}{\alpha}, \quad \tilde{t} = \frac{t - t_c}{\sqrt{2/\alpha}},$$

$$F(\tilde{t}) = \frac{1}{\pi} \left| \int_{-\infty}^{\tilde{t}} e^{i\eta^2} d\eta \right|^2 = \frac{1}{4} \left| 1 + \text{erf} \left(\frac{\tilde{t}}{\sqrt{i}} \right) \right|^2. \quad (41)$$

Notice that the function $F(\tilde{t})$ with \tilde{t} proportional to a spatial coordinate describes the Fresnel diffraction²³ and has the following asymptotic dependence:

$$F(\tilde{t}) \approx 1 + \frac{\sin(\tilde{t}^2 - \pi/4)}{\sqrt{\pi} \tilde{t}} \quad \text{for } \tilde{t} \gg 1, \quad (42a)$$

$$F(\tilde{t}) \approx (4\pi \tilde{t}^2)^{-1} \quad \text{for } -\tilde{t} \gg 1. \quad (42b)$$

The oscillating term in Eq. (42a) describes the beating between the oscillator and driving force frequencies, with the difference frequency increasing in time, $d(\tilde{t}^2)/dt = \alpha(t - t_c)$, and amplitude of beating decreasing as $1/\tilde{t}$ (see dashed line in Fig. 6a). Notice that $F(0) = 1/4$, $F(\infty) = 1$, and the maximum value is $F(1.53) = 1.370$, so that E_0 is the long-time limit of the oscillator energy

E_2 , while the maximum energy is 1.37 times larger:

$$E_{2,\max} = \frac{1.37\pi\zeta^2 m'' A^2}{\alpha}. \quad (43)$$

This result for the energy can be understood in the following way. In case of exact resonance, the oscillation amplitude of $x(t)$ in Eq. (38) increases linearly in time with the rate¹¹ $\zeta A/\omega_{l2}$. The effective time of resonance Δt corresponds to a significant phase shift due to beating: $\alpha(\Delta t)^2 \sim 1$. Therefore the resulting amplitude after the resonance crossing is $\sim \zeta A/\omega_{l2}\sqrt{\alpha}$ and the corresponding energy is $E_2 \sim \zeta^2 m'' A^2/\alpha$, which coincides with Eq. (43) up to a numerical factor.

For the parameters of Fig. 6 ($N_{l2} = 5$) we find from Fig. 5 that exact resonance between $f_d(t)$ and $\omega_{l2}/2\pi = 8.91$ GHz occurs at $t_c = 0.085 T_1$ (in particular, $t_c = 2.13$ ns for $T_1 = 25$ ns and $t_c = 43$ ns for $T_1 = 500$ ns), and $\alpha = 110 \text{ ns}^{-1}/T_1$. [For comparison, for $N_{l2} = 10$ (so that $\omega_{l2}/2\pi = 10.2$ GHz), we find from Fig. 5 $t_c = 0.192 T_1$ (i.e., $t_c = 4.8$ ns for $T_1 = 25$ ns and $t_c = 96$ ns for $T_1 = 500$ ns), and $\alpha = 57 \text{ ns}^{-1}/T_1$.] Using Eq. (43) with $A = A(t_c) = 4.3 \times 10^3 \text{ ns}^{-2}$ (see Sec. III) we find the maximum energy $E_{2,\max}/\hbar\omega_{l2}$ for $C_x = 5 \text{ fF}$ to be 11.8 for $T_1 = 25$ ns and 235 for $T_1 = 500$ ns. These values somewhat differ from the numerical results shown in Fig. 6(a) and (b) (14.2 and 242, respectively). The analytical time dependence of the energy $E_2(t)$ given by Eq. (41) for $C_x=5 \text{ fF}$ and $T_1=25 \text{ ns}$ is shown by the dashed line in Fig. 6(a). Figure 6(a) shows that Eq. (41) corresponds fairly well to the numerical solution. The discrepancy can be attributed mainly to the fact that A and α change with time, in contrast to the assumptions made in the derivation of Eqs. (41). Note also, for comparison, the case $N_{l2} = 10$, when, for instance, for $T_1 = 500$ ns and $C_x = 5 \text{ fF}$, the maximum value of $E_{2,\max}/\hbar\omega_{l2}$ is 610. This is close to the result of Eq. (43), $E_{2,\max}/\hbar\omega_{l2} = 580$, obtained on the account that now $A = A(t_c) = 5.2 \times 10^3 \text{ ns}^{-2}$ (see Sec. III). In the present case, $E_{2,\max}$ is more than 2 times greater than the maximum shown in Fig. 6(b) for the same values of T_1 and C_x . This can be explained by the fact that now α is smaller and A is greater than in the case $N_{l2} = 5$.

So far we have completely neglected the energy relaxation in the second qubit. Since the effective time of resonance is $\Delta t \sim 3/\sqrt{\alpha}$ [rise time of the function $F(\tilde{t})$ from the 10% level to the maximum], the neglected effect should not be important (less than $\sim 10\%$) for $T_1 \gtrsim 30/\sqrt{\alpha}$. Using the estimate $\alpha = 120 \text{ ns}^{-1}/T_1$ (see above), we find that taking into account the second qubit relaxation would not change significantly our results for $E_{2,\max}$ in the case $T_1 \gtrsim 10 \text{ ns}$, which justifies our model.

Let us discuss the dependence of the maximum energy $E_{2,\max}$ of the second qubit on C_x and T_1 . Taking into account that $\zeta \propto C_x$ (for $C_x \ll C$) and $\alpha \propto 1/T_1$, we obtain from Eq. (43) the scaling

$$E_{2,\max} \propto C_x^2 T_1. \quad (44)$$

As seen from Fig. 6, numerical results confirm the obvious

scaling $E_{2,\max} \propto C_x^2$, while the scaling $E_{2,\max} \propto T_1$ is not very accurate, but is still good as a first approximation.

In this subsection we have treated the second qubit as a classical harmonic oscillator. However, to analyze the measurement error due to the crosstalk, we have to assume switching from the left well to the right well when $E_{2,\max} > N_{l2}\hbar\omega_{l2}$ (which is surely not fully consistent with the oscillator model). All curves in Fig. 6 ($N_{l2} = 5$) correspond to such switching, leading to the measurement error. The measurement error can be improved by decreasing the coupling capacitance C_x , which should be chosen to be smaller for larger T_1 . Equation (44) implies that to avoid the errors due to crosstalk, one needs to choose

$$C_x < C_{x,T} = B_o/\sqrt{T_1}, \quad (45)$$

where $C_{x,T}$ is the threshold coupling capacitance. From the numerical simulations (cf. the data shown in Fig. 6), we obtain $B_o = 14.9 \text{ fF}\sqrt{\text{ns}}$ in the case $N_{l2} = 5$. For $N_{l2} = 10$ we get $B_o = 14.3 \text{ fF}\sqrt{\text{ns}}$, yielding a little stricter condition than for $N_{l2} = 5$. Notice that experimental parameters of Ref. 9 ($C_x=6 \text{ fF}$, $T_1=25 \text{ fF}$) exceed these bounds approximately twice, which is an indication that our simple model is not sufficiently accurate. As we will see in the next subsection, the theoretical bound is softer (higher) when we use actual potential profile for the second qubit instead of using the harmonic oscillator model.

B. Actual qubit potential

Let us analyze the second qubit evolution still using a classical model, but taking into account the actual potential profile $U_2(\delta_2)$, i.e., solving Eq. (37) instead of the simplified equation (38). Figures 7 and 8 show the time dependence of the second-qubit energy,

$$E_2 = m''\dot{\delta}_2^2/2 + U_2(\delta_2), \quad (46)$$

in the absence of dissipation in the second qubit ($T_1' = \infty$), for $N_{l2} = 5$ and $T_1 = 25$ and 500 ns. A comparison of Figs. 6(a) and 7 shows that in both models the qubit energy remains small before a sharp increase in energy. However, there are significant differences due to account of anharmonicity: (a) The sharp energy increase occurs earlier than in the oscillator model (the highest maximum at short times is reached in Figs. 6(a) and 7, respectively, at ≈ 3 and 2 ns); (b) The excitation of the qubit may be to a much lower energy than for the oscillator; (c) After the sharp increase, the energy occasionally undergoes noticeable upward or downward jumps, which may even overshoot the above sharp increase; (d) In contrast to the oscillator model, the qubit may now escape (switch) to the right well much later than during initial sharp energy increase (in Fig. 7(b) the escape happens at $t \simeq 44$ ns).

The properties (a) and (b) can be understood by taking into account the fact that the oscillation frequency in

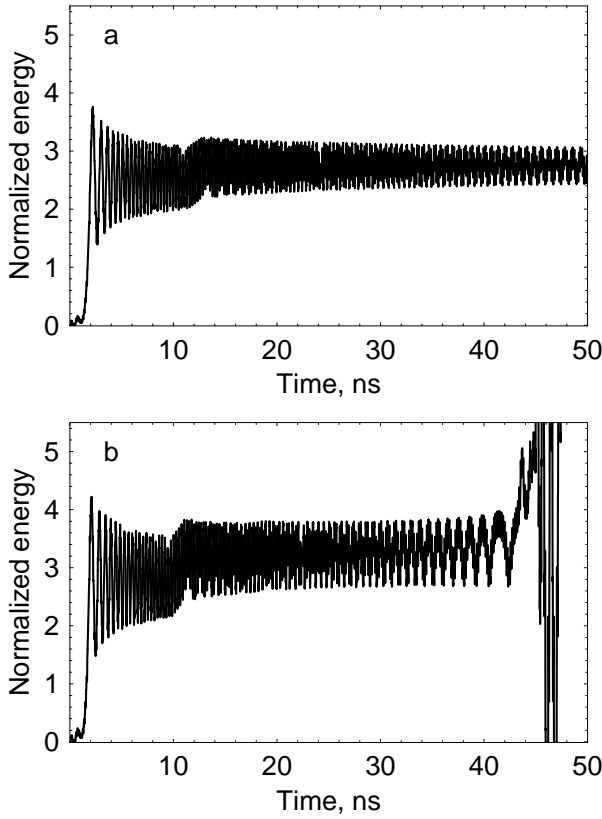


FIG. 7: The second-qubit energy E_2 (in units of $\hbar\omega_{l2}$) vs. time t (in ns) for $N_{l2} = 5$, $T_1 = 25$ ns, and (a) $C_x = 5$ fF and (b) 6 fF.

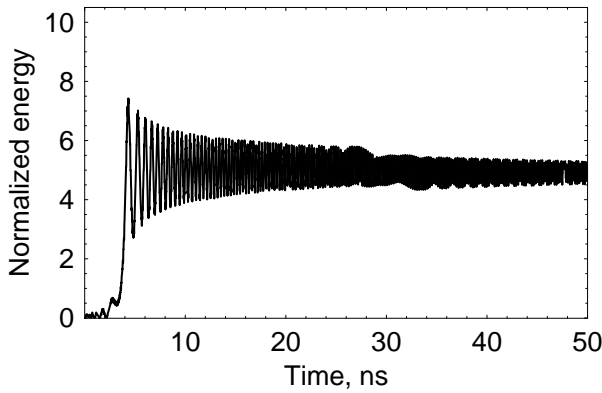


FIG. 8: The second-qubit energy E_2 (in units of $\hbar\omega_{l2}$) vs. t (ns) for $N_{l2} = 10$, $T_1 = 25$ ns, and $C_x = 6$ fF.

the second qubit *decreases* with the energy increase (it should become formally zero at the top of the barrier), while the driving frequency *increases* with time (Fig. 5). Therefore, initially small out-of-resonance beatings when $\omega_d < \omega_{l2}$ are amplified because of the positive feedback: larger amplitude makes it closer to the resonance, which increases the amplitude even more. This makes the non-excited state unstable, which leads to a sharp increase of the qubit energy earlier than the condition $\omega_d = \omega_{l2}$

is satisfied. The same mechanism is also responsible for lower qubit excitation, when compared to the harmonic oscillator model: the resonance cannot be as efficient as in the harmonic oscillator model since the qubit excitation moves the qubit frequency out of the resonance. The property (c) is related to crossing of higher-order resonances, which occur when $\omega_d(t)$ is commensurate¹¹ with the oscillation frequency of the system, which itself depends on the energy $E_2(t)$ and hence on the time.

In contrast to the oscillator model, Eq. (37) for the actual qubit potential cannot be solved analytically,²⁴ so we rely only on the numerical simulations. We are interested in the conditions, under which the system remains in the left well. Generally, the qubit excitation increases with increase of the coupling C_x ; therefore one expects a certain critical value $C_{x,T}$ (depending on T_1 and other parameters), which separates the switching and no-switching scenarios. However, because of the complex dynamics of the system, the dependence on C_x is non-monotonous, so that increasing C_x may sometimes change switching case into no-switching case. In this situation, we define $C_{x,T}$ as a minimum value at which the switching happens (even though larger C_x may correspond to no-switching). Similar to the harmonic oscillator model, we expect that $C_{x,T}$ generally decreases with increase of T_1 ; however, because of the complex dynamics, the dependence $C_{x,T}(T_1)$ should not necessarily be monotonous.

Lines 1 and 3 in Fig. 9 show the numerically calculated $C_{x,T}$ for 5 values of T_1 from 25 ns to 500 ns and for $N_{l2} = 5$ and 10 (so far we still assume $T'_1 = \infty$). For these calculations we used the increment of 0.1 fF for C_x and simulated the qubit dynamics in the time interval $0 \leq t \leq 6T_1$. Notice that the lines are not smooth (line 1 even has a bump), which is the result of irregular nonlinear dynamics of the system. Nevertheless, lines 1 and 3 confirm the generally decreasing dependence $C_{x,T}(T_1)$, and fitting them by the formula

$$C_{x,T}(T_1) \simeq BT_1^{-\beta}, \quad (47)$$

(where $C_{x,T}$ is measured in fF while T_1 is measured in ns) we obtain $B \simeq 8$ and 12 for $N_{l2} = 5$ and 10, respectively, whereas $\beta \simeq 0.12$ for the both lines.

Since the gate speed is proportional to C_x , it is advantageous to have higher C_x . The above results show that raising the barrier after the measurement pulse to $N_{l2} = 10$ allows to increase C_x in comparison with the case $N_{l2} = 5$. The reason for this is illustrated by the comparison of Figs. 7(b) and 8, which shows that for the case $N_{l2} = 10$ (see Fig. 8) the sharp energy increase is lower relative to the barrier top than for $N_{l2} = 5$ (Fig. 7(b)). Note that the dependence (47) is much weaker than the relation $C_x \propto T_1^{-1/2}$ obtained in the oscillator model, which is advantageous for design of qubits with weak decoherence (large T_1).

Now let us consider the effect of dissipation in the second qubit. The dashed line 2 in Fig. 9 shows $C_{x,T}(T_1)$ in the presence of dissipation ($T'_1 = T_1$) and the same

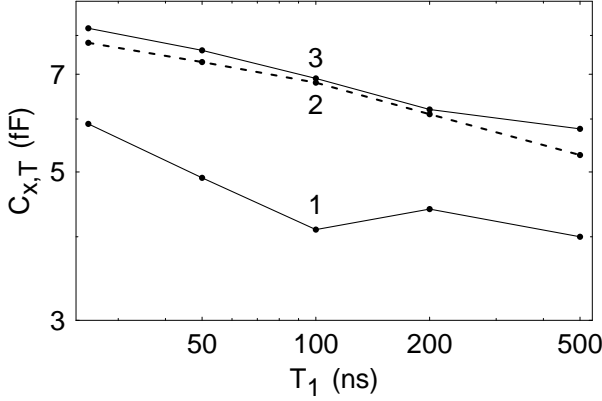


FIG. 9: The log-log plot of the critical value $C_{x,T}$ vs. T_1 for $N_{l2} = 5$ (lines 1 and 2) and 10 (line 3); $T'_1 = \infty$ for lines 1 and 3 and $T'_1 = T_1$ for line 2. The numerical data are shown by the dots connected by lines for clearness.

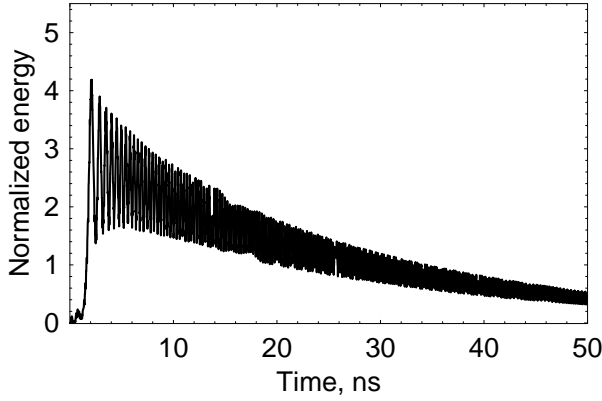


FIG. 10: The second-qubit energy $E_2(t)$ (in units of $\hbar\omega_{l2}$) in the presence of dissipation in the second qubit, for $N_{l2} = 5$, $C_x = 6$ fF, and $T'_1 = T_1 = 25$.

other parameters as for line 1 (for which $T'_1 = \infty$). As we see, account of dissipation increases $C_{x,T}$ quite noticeably, which contradicts the conclusion from the harmonic oscillator model (predicting no significant dependence). The reason is that for C_x slightly above $C_{x,T}$ the switching in the model without dissipation usually occurs significantly later than the initial sharp increase of the energy [Fig. 7(b)] and is caused by “secondary” slight jumps of the energy caused by strongly nonlinear dynamics, as discussed above. Dissipation in the second qubit shortens significantly the time interval where the switching due to secondary jumps is possible (Fig. 10), thus increasing $C_{x,T}$. Note a possibility of a return of the system to the left well after the escape into the right well, which may take place with or without dissipation. Fitting the dashed line in Fig. 9 by the power-law dependence (47), we find $B \simeq 12$ and $\beta \simeq 0.13$, so that the scaling power β is practically the same as in the no-dissipation case, while B is considerably larger.

V. SECOND QUBIT: QUANTUM APPROACH

In the quantum approach the second qubit is described by the wave function $\Psi(\delta, t)$ (henceforth we will omit the subscript 2), which obeys the Schroedinger equation

$$i\hbar \frac{\partial \Psi}{\partial t} = H(t)\Psi. \quad (48)$$

Here the Hamiltonian

$$H(t) = \frac{\hat{p}^2 + 2\zeta p_1(t)\hat{p}}{2(1 + \zeta)m} + U(\delta) \quad (49)$$

(where $\hat{p} = -i\hbar\partial/\partial\delta$) follows from Eq. (31) by considering p_2 as the operator \hat{p} and p_1 and δ_1 as classical functions of time obtained from Eqs. (34), (33) and by neglecting the term equal to the first-qubit energy.

The term linear in \hat{p} in Eq. (49) has the form of that resulting from the interaction of a charged particle with a time-dependent electric field described by a vector potential.²³ Using the gauge transformation²⁵

$$\Psi(\delta, t) = \Psi'(\delta, t)e^{-i\zeta p_1(t)\delta/\hbar}, \quad (50)$$

we can replace the vector-potential by a scalar potential in the Hamiltonian. Then Eq. (48) becomes

$$i\hbar \frac{\partial \Psi'}{\partial t} = H'(t)\Psi', \quad (51)$$

where

$$H'(t) = H_0 + V(t), \quad (52)$$

$$H_0 = \frac{\hat{p}^2}{2m''} + U(\delta), \quad V(t) = -\zeta m'' \ddot{\delta}_1(t)\delta.$$

In the last equality Eq. (33) was used. To obtain Eq. (51), we neglected a small c -number term $\zeta^2 p_1^2(t)/(2m'')$.

The partial differential equation (51) can be reduced to an infinite set of ordinary differential equations,²⁵ using the expansion of the wavefunction over the eigenfunctions $\psi_n(\delta)$ of H_0 ,

$$\Psi'(\delta, t) = \sum_n a_n(t)\psi_n(\delta). \quad (53)$$

Inserting expansion (53) into Eq. (51) yields the set of equations for the coefficients $a_n(t)$

$$\dot{a}_n = -i(E_n/\hbar)a_n + \frac{i\zeta m'' \ddot{\delta}_1(t)}{\hbar} \sum_{n'} \delta_{nn'} a_{n'}, \quad (54)$$

where E_n is an eigenvalue of H_0 and

$$\delta_{nn'} = \int_{-\infty}^{\infty} \psi_n^*(\delta)\delta\psi_{n'}(\delta)d\delta. \quad (55)$$

Alternatively, one can recast Eq. (49) as $H(t) = H_0 + V'(t)$, where $V'(t)$ is the term linear in \hat{p} , and derive equations similar to (54). Note, however, that when the

vector potential does not vanish, the generalized momentum \hat{p} differs from the kinetic momentum $m''\hat{\delta}$ and hence H_0 [Eq. (52)] is not the energy operator [cf. the classical energy (46)]. Thus, the gauge with the vanishing vector potential has the advantage that, in contrast to other gauges, the coefficients of $\psi_n(\delta)$ in the expansion of the wave function has the physical meaning of the probability amplitudes of the energy eigenstates.²⁶

The eigenstates and eigenvalues of H_0 have been obtained numerically, using the Fourier grid Hamiltonian²⁷ (or, equivalently, periodic pseudospectral²⁸) method. The eigenfunctions being known, one can calculate the matrix $\delta_{nn'}$ (55) and solve numerically Eqs. (54) for a final subset of the states. For a given N_l , we take a reasonably small number n_s of consecutive states ($n = n_i, n_i + 1, \dots, n_i + n_s$), which include the left-well states and provide a sufficient approximation to the solution (the choice of the subset of states is discussed below). The column vector $a = (a_{n_i}, \dots, a_{n_i + n_s})^T$ satisfies the equation [cf. (54)]

$$i\hbar\dot{a} = \tilde{H}(t)a. \quad (56)$$

Here the matrix

$$\tilde{H}_{nn'}(t) = E_n \delta_{nn'}^K - \zeta m'' \ddot{\delta}_1(t) \delta_{nn'} \quad (n_i \leq n, n' \leq n_i + n_s), \quad (57)$$

(where $\delta_{nn'}^K$ is the Kronecker symbol) is the Hamiltonian of the system in the restricted Hilbert space spanned by the subset.

We define the probability $P_l(t)$ to find the system in the left well by

$$P_l(t) = \sum_{n_l} P_{n_l}(t), \quad P_n(t) = |a_n(t)|^2. \quad (58)$$

Here $P_n(t)$ is the probability of state n and the summation is over the states localized in the left well. We will also denote $P_{n_l}(t)$ by $Q_k(t)$, where k numerates the states in the left well, starting from $k = 0$ (the ground state). We define the switching probability by $P_s(t) = 1 - P_l(t)$.

Figure 11 shows (for the case $N_l = 10$) the eigenfunctions $|\psi_n(\delta)|^2$ and the corresponding energies E_n for $145 \leq n \leq 171$, where n is the level quantum number, such that $n = 0$ denotes the ground state. One can see 3 types of states: (a) 12 states localized in the left well ($n = 146, 148, \dots, 166, 169$ or, respectively, $k = 0, \dots, 11$), (b) delocalized states ($n \geq 170$), and (c) states localized in the right well (the remaining states). Depending on the barrier height (or the external flux ϕ) there may appear also resonant states: when the energies of states localized in the left and right wells approach sufficiently, the states mix with each other and become delocalized. Actually, in Fig. 11 the left-well states $k = 10$ and 11 are partially delocalized due to the interaction with neighboring right-well states.

Figure 12 shows the left-well population $P_l(t)$ for $N_l = 10$ and $T_1 = 25$ ns. The subset of the states used in this calculation is $141 \leq n \leq 185$. Figure 13 shows the

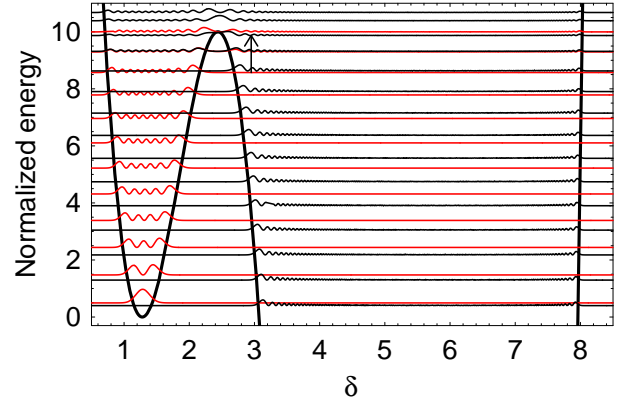


FIG. 11: (Color online) Potential $U(\delta)$ (the thick line) and eigenfunctions $|\psi_n(\delta)|^2$ ($145 \leq n \leq 171$), shifted vertically by the value of E_n (in units of $\hbar\omega_l$) for $N_l = 10$ and $C_x = 6$ fF. The energy origin is chosen at the minimum of the left well.

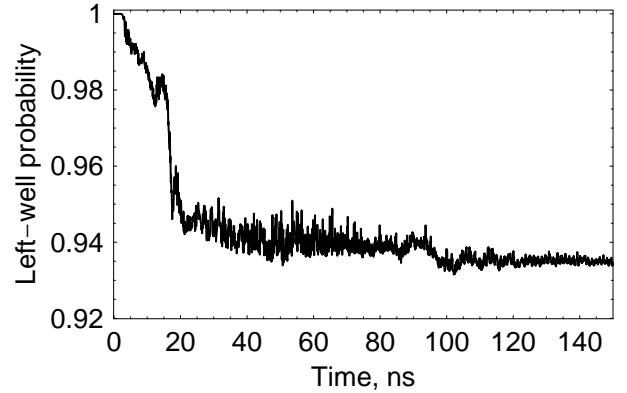


FIG. 12: The left-well probability $P_l(t)$ for $N_l = 10$, $C_x = 6$ fF, and $T_1 = 25$ ns.

populations of the first 10 levels in the left well; the populations of levels $k = 11$ and 12 are not shown since they are very close to zero.

Figure 14 shows the qubit mean energy,

$$\bar{E}(t) = \sum_n E_n P_n(t). \quad (59)$$

It can be compared with the classical qubit energy (Fig. 8) obtained for the same parameters as in Figs. 12 and 13. The two curves are roughly similar. Note, however, that the mean energy starts at $t = 0$ from a nonzero value equal to the qubit energy in the ground state $\approx \hbar\omega_l/2$. Though the mean energy, similarly to the classical energy, is significantly lower than the barrier height, the escape (switching) probability $P_s(t) = 1 - P_l(t)$ is nonzero in the quantum case (see Fig. 12).

The switching time dependence (Fig. 12) looks quite irregular. This shows that the quantum behavior is rather complicated, which is reminiscent of its classical analog discussed in Sec. IV B. According to Figs. 13 and 14, for $t < 3$ ns, the driving force is far from the resonance with

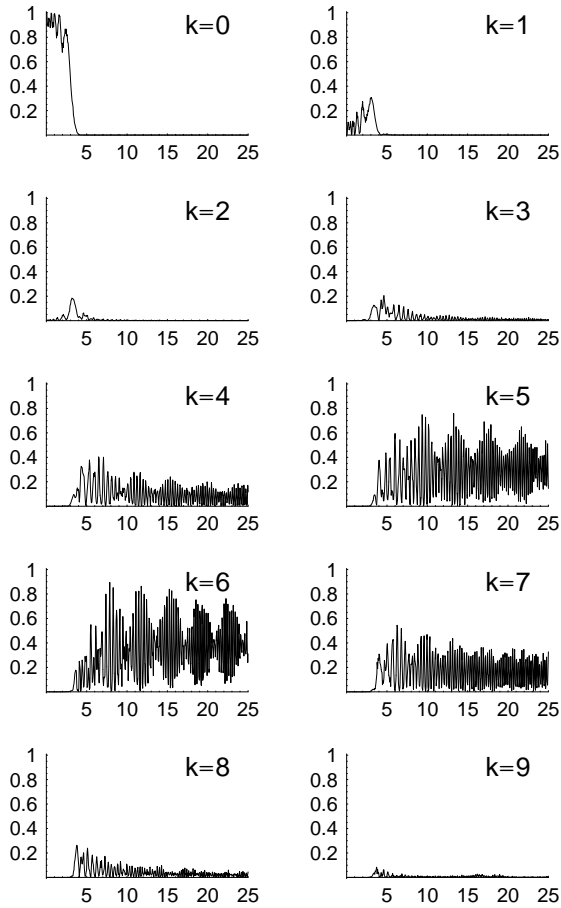


FIG. 13: The left-well probabilities $Q_k(t)$ vs. t (ns) for $N_l = 10$, $C_x = 6$ fF, and $T_1 = 25$ ns.

the qubit, and population mainly remains in the ground state. At this stage, there is no switching (see Fig. 12). At $3 \lesssim t \lesssim 4$ ns, there occurs a fast excitation, in a manner reminiscent of the classical case (Sec. IV B). To understand the excitation mechanism, we show in Fig. 15 the Rabi frequencies $R_{k,k-1} = \zeta m'' A |\delta_{k,k-1}| / \hbar$ of the adjacent left-well transitions, i.e., the amplitude of the resonant component of $V_{k,k-1}(t) / \hbar$ [cf. Eq. (52)]. In Fig. 15, as in Sec. IV B, we adopt $A = A(t_c) = 5.2 \times 10^3$ ns $^{-2}$. For not too high levels, one can use the harmonic-oscillator relation²⁵ $|\delta_{k,k-1}| \approx \sqrt{k\hbar/2m''\omega_{2l}} = 0.10\sqrt{k}$, yielding $R_{k,k-1}/2\pi \approx A(C_x/C)\sqrt{mk/2\hbar\omega_{2l}}/2\pi = 0.53\sqrt{k}$ MHz. Figure 16 shows the time dependence of the corresponding detunings $\omega_{k,k-1} - \omega_d(t)$. Though the resonance with the transition 1-0 occurs at $t = 4.3$ ns, the excitation begins earlier, at $t \approx 3$ ns, when $\omega_{10} - \omega_d(t) \sim R_{10} \approx 0.5$ GHz. Since the Rabi frequencies increase with k , whereas the detunings first decrease and then increase with k , the ground level population propagates promptly to higher levels, until the detunings become so large that the excitation stops. At $t > 4$ ns levels 0-2 become empty, whereas almost all the population is transferred to levels

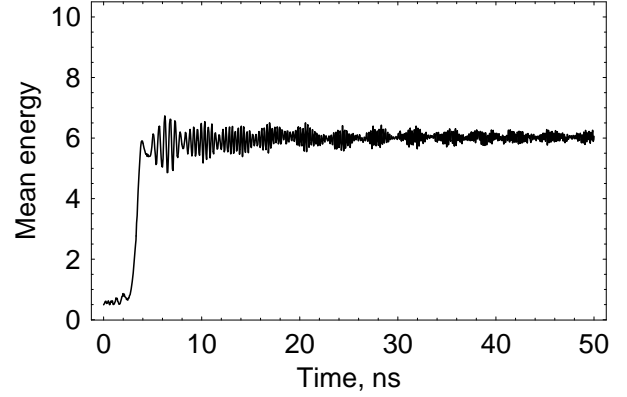


FIG. 14: The mean qubit energy (59) in units of $\hbar\omega_l$ for $N_l = 10$, $C_x = 6$ fF, and $T_1 = 25$ ns.

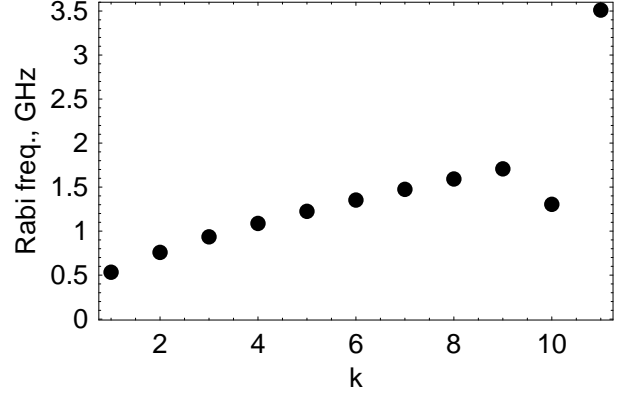


FIG. 15: Rabi frequencies $R_{k,k-1}/2\pi$ of the left-well transitions for $N_l = 10$, $C_x = 6$ fF, and $T_1 = 25$ ns.

4-7.

The escape (switching) in the quantum case can occur in several ways. The population which goes to two highest states $k = 10$ and 11 is lost rather fast, since those states interact significantly with the right-well and delocalized states. With the increase of the driving frequency $\omega_d(t)$, it can become resonant with transitions between non-adjacent states, providing thus a possible mechanism of switching. Note that for $k \leq 8$ the matrix elements of $V(t)$ between the left and right wells are very small, which actually precludes direct switching from states $k \leq 8$. In contrast, state $k = 9$ has noticeable matrix elements with states outside the left well. In particular, more than half of the switching probability is obtained due to the sharp decrease of $P_l(t)$ at $t = 16$ ns ($t < 16$ ns) and the transition between state $k = 9$ ($n = 164$) and the right-well state $n = 168$ with the frequency 13.2 GHz (see the arrow in Fig. 11). At $t = 16$ ns the detuning for this transition is 0.7 GHz, which is much smaller than other detunings between levels of interest and is comparable to the corresponding Rabi frequency ≈ 0.3 GHz. The latter value can be obtained as in the previous paragraph,

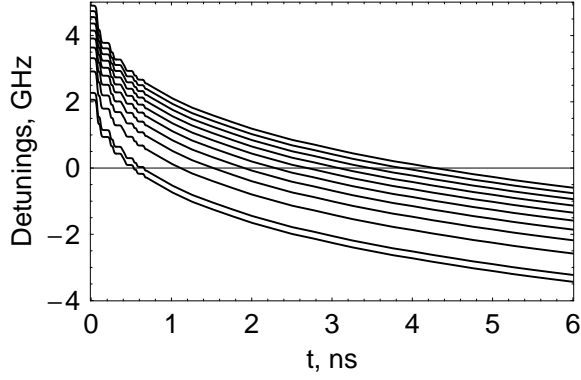


FIG. 16: Detunings $(\omega_{k,k-1} - \omega_d(t))/2\pi$ of left-well transitions for $N_l = 10$, $C_x = 6$ fF, and $T_1 = 25$ ns. Curves from top to bottom correspond to $k = 1, \dots, 11$.

taking into account that $A(t = 16 \text{ ns}) = 5.8 \times 10^3 \text{ ns}^{-2}$ and $|\delta_{164,168}| = 0.048$.

Another possible escape mechanism is tunneling through the barrier. To get an insight into the tunneling mechanism, note that, as follows from Eqs. (52) and (2), the perturbation $V(t)$ is equivalent to the substitution in H_0

$$\phi \rightarrow \phi + \zeta \lambda m'' \ddot{\delta}_1(t) / E_J \quad (60)$$

[with the accuracy to a small term $\zeta^2 \lambda m''^2 \ddot{\delta}_1^2(t) / (2E_J)$ in $H'(t)$]. Thus, the crosstalk perturbation can be described as an oscillating modulation of the external magnetic flux. As a result, N_l varies from 9.15 to 11.2, which correspond, respectively, to the maximum and minimum of $\ddot{\delta}_1(t)$: $9 \times 10^{21} \text{ s}^{-2}$ and $-13 \times 10^{21} \text{ s}^{-2}$. (Note that the above extrema of oscillations of $\ddot{\delta}_1(t)$ remain constant in the time interval $0 \leq t \leq 0.4T_1$, since they correspond to the points of inflection δ'_c and $\delta_c + 2\pi$ of $U(x)$ [see Eq. (7)], as long as these points lie between the extrema of $\delta_1(t)$.) Due to the variation of N_l with t , each left-well level crosses with several right-well levels during one oscillation cycle. These (avoided) crossings lead to transitions between the states in different wells (tunneling), the rate of which, according to the Landau-Zener formula,²⁵ is $\sim W^2$, where W is the minimal level splitting at the crossing. The values of W increase exponentially with the decrease of N_l and the increase of k . Therefore, the tunneling is a relatively slow (ineffective) switching mechanism for all levels, except for the highest ones (such as $k = 11$ and 10).

Calculations of the switching probability $P_s(t)$ have been performed for different values of the parameters C_x , T_1 , and N_l , in the time interval $[0, 6T_1]$. After the time $6T_1$ the first-qubit oscillations decay to a very low level, and, respectively, the perturbation of the second qubit is weak, so that the change of $P_s(t)$ for $t > 6T_1$ is assumed to be negligible. For $N_l = 5$, Eqs. (54) were solved for the subset $167 \leq n \leq 196$. In this case, there are 6 states localized in the left well ($n = 169, 171, \dots, 179$).

Let us briefly discuss our choice of the subset of states

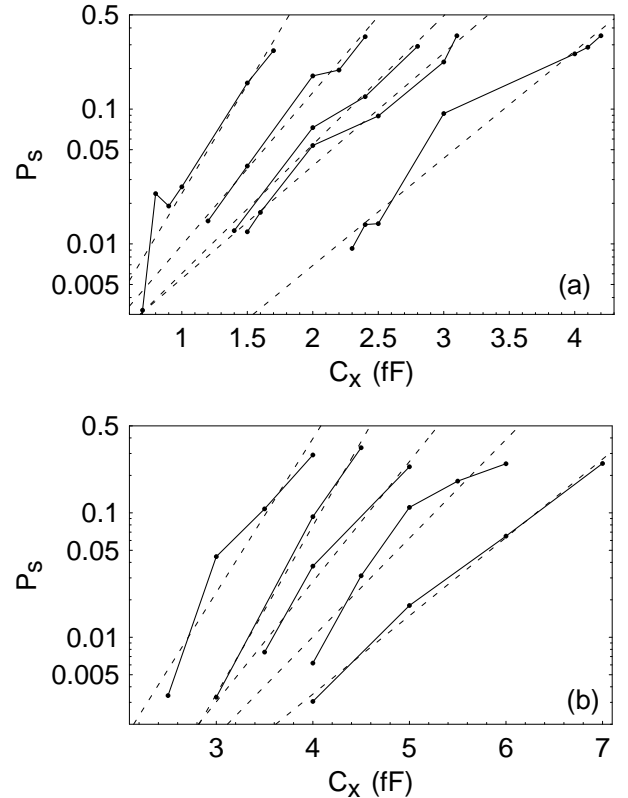


FIG. 17: The switching probability $P_s(6T_1)$ vs. C_x (fF) in the logarithmic scale for $T_1 = 25, 50, 100, 200$, and 500 ns (respectively, the lines from right to left) for (a) $N_l = 5$ and (b) $N_l = 10$. The numerical data are represented by the points, connected by solid lines for clearness; the dashed straight lines are results of the least-squares fit.

employed for the numerical solution of Eq. (56). One of the requirements is the following. We consider the eigenvalues of $\tilde{H}_{nn'}$ (57) as functions of $\ddot{\delta}_1$ and require that the latter dependence be sufficiently close to its counterpart obtained by the exact Hamiltonian (52). We have required also that the matrix $\delta_{nn'}$ in the representations, where $\tilde{H}_{nn'}$ with the minimal and maximal values of $\ddot{\delta}_1$ is diagonal, approximately coincides with $\delta_{nn'}$ obtained from the exact Hamiltonian (52) at the same values of $\ddot{\delta}_1$. We have performed calculations with enlarged subsets (up to $n_s = 150$) and found that the switching probability varies irregularly with the number of states in the subset, but this variation is not significant, at least in the case of the present interest when the switching probability $P_s \leq 0.3$.

The results of numerical simulations are shown in Fig. 17. The lines obtained by connecting the data points are not completely smooth and are sometimes even non-monotonic. This may be explained by complicated dynamics, reminiscent of the irregular behavior in the classical case. However, the switching probability decreases approximately exponentially with C_x in all cases in Fig. 17.

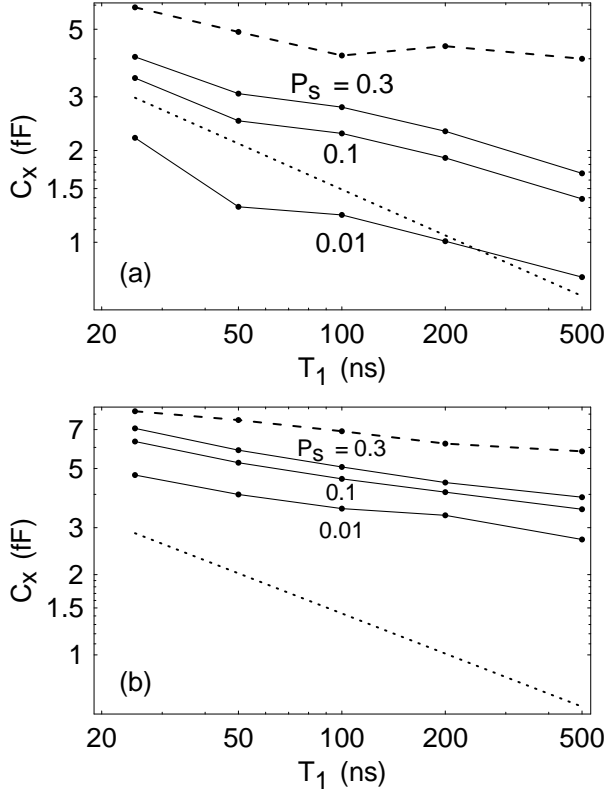


FIG. 18: Log-log contour plots for the values of the switching probability $P_s = 0.01, 0.1$, and 0.3 in the plane of C_x (in fF) and T_1 (in ns) in the quantum model for (a) $N_l = 5$ and (b) $N_l = 10$. The results for $C_{x,T}(T_1)$ in the classical models are shown by the dashed lines (actual potential model) and the dotted lines [oscillator model, Eq. (45)]. The numerical data are represented by the points, connected by lines for clearness.

Using the linear fit for the results shown in Fig. 17, we obtain the contour plot for $P_s = P_s(6T_1)$ versus C_x and T_1 (see the solid lines in Fig. 18). The data for P_s in Fig. 18 can be fitted by straight lines, yielding approximate dependencies $C_x(T_1)$ in the form similar to (47),

$$C_x(T_1) \approx B(P_s)T_1^{-\beta(P_s)}. \quad (61)$$

The values of the parameters for this formula are shown in Table I. Note that β depends weakly on P_s , but decreases appreciably when N_l increases from 5 to 10. The values of β in Table I appear to be greater than the value $\beta = 0.12$ obtained for the classical model (Sec. IV B), but less than power 0.5 in the oscillator model [Eq. (45)], i.e., the T_1 dependence in Eq. (61) is intermediate between those found in the oscillator and actual-potential classical approaches. Figure 18 also shows a comparison of the results of classical and quantum approaches. As one can see, both oscillator and actual-potential classical models give the limits for C_x roughly similar to quantum results (within a factor of ~ 2), with the exception of the case of the oscillator model for $N_l = 10$ and $T_1 > 100$ ns.

These results can be used for the design of phase-qubit-based quantum gates. In particular, they give us the

N_l	5			10		
P_s	0.01	0.1	0.3	0.01	0.1	0.3
B	5.4	8.3	9.7	8.1	11	13
β	0.32	0.29	0.28	0.18	0.19	0.20

TABLE I: Parameters of Eq. (61) for the quantum model (C_x is in fF and T_1 is in ns), limiting the coupling capacitance C_x for several values of the error probability P_s and dimensionless barrier height N_l .

maximum allowed coupling capacitance C_x and hence the maximum gate operation speed, for a particular tolerable value of the error due to crosstalk. An important result of the quantum treatment is the exponential dependence of the error probability on C_x and a rather slow dependence on T_1 , that shows the possibility of fabrication of phase-qubit-based quantum gates with low decoherence and with a sufficiently high operation speed.

The present theory does not take into account dissipation in the second qubit. The dissipation may shorten the effective crosstalk time and thus decrease the crosstalk error (the switching probability), similar to the classical case discussed in Sec. IV B. Thus, the present results give a lower bound on the maximum allowed C_x . Taking into account the results of the classical model, one may expect $\sim 30\%$ larger limit for the coupling capacitance for a quantum model with energy dissipation in the second qubit.

VI. CONCLUSIONS

The main goal of the present paper has been to study the crosstalk between two capacitively coupled flux-biased phase qubits after the measurement pulse. The first qubit, which has escapes (switches) from the left to the right well during the pulse, has been modeled classically. The first qubit performs damped oscillations (with energy relaxation time T_1) with increasing in time frequency $f_d(t)$; these oscillations perturb the capacitively coupled second qubit. The dynamics of the second qubit (which is initially in the ground state) has been treated both classically and quantum-mechanically.

In the classical treatment of the second qubit, we have compared the previously suggested⁹ oscillator model, which allows for both analytical and numerical analysis, with the model based on the exact potential, which can be solved only numerically. Both models show a sharp resonant excitation of the second qubit at a time short in comparison with T_1 . Though there is a certain similarity between the two approaches, they significantly differ both quantitatively and qualitatively. In contrast to the oscillator model, the exact-potential model shows nonlinear and irregular dynamics. The second qubit remains in the left well when the coupling capacitance is sufficiently low, $C_x \leq C_{x,T}$, but may escape (though not certainly because of complicated dynamics) if $C_x > C_{x,T}$. We have

obtained numerically the dependence $C_{x,T}(T_1)$ both in absence and presence of dissipation in the second qubit for several values of the barrier height.

For the quantum treatment we have developed an efficient numerical scheme, which employs a subset of eigenstates of the unperturbed Hamiltonian. In this case, similarly to the classical case, a fast excitation of the second qubit occurs at a moment when the perturbation frequency $f_d(t)$ is somewhat below the transition frequency between the ground and first excited states. However, in contrast to the classical case, the switching can now occur when the qubit mean energy is significantly lower than the barrier height, due to tunneling. Another switching mechanism is the excitation above the barrier. The switching probability generally increases with time, but the time dependence is irregular, containing oscillations and jumps (similar jumps due to complicated dynamics also occur in the classical model).

The results for the switching (error) probability P_s have been presented as contour plots on the plane of cou-

pling capacitance C_x and relaxation time T_1 (Fig. 18). Such plots may be important for the design of quantum gates based on phase qubits. Comparison of the results obtained in the quantum and classical models shows that the classical models can be used for a crude estimate of the crosstalk error; however, the difference becomes significant for $T_1 \gtrsim 100$ ns. In the quantum approach the dissipation in the second qubit have been neglected. However, by analogy with the classical case, one can expect that the account of dissipation will not change the results significantly, though it will somewhat increase the upper bound for the coupling capacitance, above which the crosstalk error becomes intolerable.

The present study can be of relevance for problems in other fields (i.e., laser chemistry), which consider excitation into or escape from a potential well by an oscillating driving force with changing in time parameters.

The work was supported by NSA and DTO under ARO grant W911NF-04-1-0204.

* Permanent address: Department of Chemical Physics, The Weizmann Institute of Science, Rehovot 76100, Israel

¹ J. M. Martinis, S. Nam, J. Aumentado, and C. Urbina, Phys. Rev. Lett. **89**, 117901 (2002); Y. Yu, S. Han, X. Chu, S.-I Chu, and Z. Wang, Science **296**, 1869 (2002); A. J. Berkley, H. Xu, R. C. Ramos, M. A. Gubrud, F. W. Strauch, P. R. Johnson, J. R. Anderson, A. J. Dragt, C. J. Lobb, and F. C. Wellstood, Science **300**, 1548 (2003).

² I. Chiorescu, Y. Nakamura, C. J. P. M. Harmans, and J. E. Mooij, Science **299**, 1869 (2003); J. R. Friedman, V. Patel, W. Chen, S. K. Tolpygo, and J. E. Lukens, Nature **406**, 43 (2000).

³ Y. Nakamura, Yu. A. Pashkin, and J. S. Tsai, Nature **398**, 786 (1999); D. Vion D, A. Aassime, A. Cottet, P. Joyez, H. Pothier, C. Urbina, D. Esteve, and M. H. Devoret, Science **296**, 886 (2002); T. Yamamoto, Yu. A. Pashkin, O. Astafiev, Y. Nakamura, and J. S. Tsai, Nature **425**, 941 (2003); T. Duty, D. Gunnarsson, K. Bladh, and P. Delsing, Phys. Rev. B **69**, 140503 (2004); A. Guillaume, J. F. Schneideman, P. Delsing, H. M. Bozler, and P. M. Echternach, Phys. Rev. B **69**, 132504 (2004); A. Wallraff, D. I. Schuster, A. Blais, L. Frunzio, J. Majer, M. H. Devoret, S. M. Girvin, and R. J. Schoelkopf, Phys. Rev. Lett. **95**, 060501 (2005).

⁴ M. A. Nielsen and I. L. Chuang, *Quantum Computation and Quantum Information* (Cambridge University Press, Cambridge, 2000).

⁵ R. W. Simmonds, K. M. Lang, D. A. Hite, S. Nam, D. P. Pappas, and J. M. Martinis, Phys. Rev. Lett. **93**, 077003 (2004).

⁶ K. B. Cooper, M. Steffen, R. McDermott, R. W. Simmonds, S. Oh, D. A. Hite, D. P. Pappas, and J. M. Martinis, Phys. Rev. Lett. **93**, 180401 (2004).

⁷ P. R. Johnson, W. T. Parsons, F. W. Strauch, J. R. Anderson, A. J. Dragt, C. J. Lobb, and F. C. Wellstood, Phys. Rev. Lett. **94**, 187004 (2005); *ibid.* **95**, 049901 (2005).

⁸ J. Kempe and K. B. Whaley, Phys. Rev. A **65**, 052330 (2002).

⁹ R. McDermott, R. W. Simmonds, M. Steffen, K. B. Cooper, K. Cicak, K. D. Osborn, S. Oh, D. P. Pappas, and J. M. Martinis, Science **307**, 1299 (2005).

¹⁰ K. K. Likharev, *Dynamics of Josephson Junctions and Circuits* (Gordon and Breach, New York, 1986); T. Van Duzer and C. W. Turner, *Principles of Superconductive Devices and Circuits* (Elsevier, New York, 1981); A. Barone and G. Paternò, *Physics and Applications of the Josephson Effect* (Wiley, New York, 1982).

¹¹ L. D. Landau and E. M. Lifshitz, *Mechanics* (Pergamon Press, Oxford, 1976).

¹² P. R. Johnson, F. W. Strauch, A. J. Dragt, R. C. Ramos, C. J. Lobb, J. R. Anderson, and F. C. Wellstood, Phys. Rev. B **67**, 020509 (2003).

¹³ For coupled current-biased phase qubits, this Hamiltonian was obtained, e.g., in Refs. 12,14,15; similar Hamiltonian for coupled charge qubits was obtained, e.g., in Ref. 16.

¹⁴ A. Blais, A. Maassen van den Brink, and A. M. Zagoskin, Phys. Rev. Lett. **90**, 127901 (2003).

¹⁵ T. Wu, Z. Li, and J. Liu, Jap. J. Appl. Phys. **45**, L180 (2006).

¹⁶ Yu. A. Pashkin, T. Yamamoto, O. Astafiev, Y. Nakamura, D. V. Averin, and J. S. Tsai, Nature **421**, 823 (2003).

¹⁷ The chosen unrounded value for N_{l1} corresponds to a rounded value for another parameter $[(\phi_c - \phi_1)/\lambda]$ which we used in the code.

¹⁸ K. K. Likharev, Physica **108B**, 1079 (1981).

¹⁹ M. C. Gutzwiller, *Chaos in Classical and Quantum Mechanics* (Springer, New York, 1990).

²⁰ F. M. Lewis, Trans ASME **54**, 253 (1932); J. Kevorkian, SIAM J. Appl. Math. **20**, 364 (1971); *ibid.* **26**, 364 (1974).

²¹ M. J. Ablowitz, B. A. Funk, and A. C. Newell, Stud. Appl. Math. **52**, 51 (1973).

²² *Handbook of Mathematical Functions*, eds. M. Abramowitz and I. A. Stegun (NBS, 1964).

²³ L. D. Landau and E. M. Lifshitz, *The Classical Theory of Fields* (Pergamon, Oxford, 1975), sec. 60.

²⁴ Passage through resonance for a system with a quartic po-

tential (a Duffing oscillator) was considered in Ref. 21 and I. R. Collinge and J. R. Ockendon, SIAM J. Appl. Math. **37**, 350 (1979).

²⁵ L. D. Landau and E. M. Lifshitz, *Quantum Mechanics: Non-Relativistic Theory* (Pergamon Press, Oxford, 1977).

²⁶ W. E. Lamb, Phys. Rev. **85**, 259 (1952); K.-H. Yang, Ann. Phys. **101**, 62 (1977); C. Leubner and P. Zoller, J. Phys. B **13**, 3613 (1980); W. E. Lamb, R. R. Schliher, and M. O. Scully, Phys. Rev. A **36**, 2763 (1987).

²⁷ C. C. Marston and G. G. Balint-Kurti, J. Chem. Phys. **91**, 3571 (1989).

²⁸ B. Fornberg, *A Practical Guide to Pseudospectral Methods* (Cambridge University Press, Cambridge, 1996).